SAND2017-8481J

The Influence of Interfacial Slip on Two-Phase Flow in Rough Pores

Alec Kucala[1], Mario J. Martinez[1], Yifeng Wang[2], and David R. Noble[1]

[1]Sandia National Laboratories, Engineering Sciences Center, PO Box 5800, Albuquerque, NM, USA 87185-5820
[2]Sandia National Laboratories, Advanced Nuclear Energy Programs, PO Box 5800, Albuquerque, NM, USA 87185-5820

Key Points:

- Flow slip through a pore is characterized in terms of surface roughness and fluid properties
- Flow slip is quantified as a contact-angle-dependent effective permeability
- Roughness-induced slip flow will impact the mobility of CO_2 in geologic carbon storage for sufficiently rough pores

Corresponding author: Alec Kucala, akucala@sandia.gov

Abstract

The migration and trapping of supercritical CO_2 ($scCO_2$) in geologic carbon storage is strongly dependent on the geometry and wettability of the pore network in the reservoir rock. During displacement, resident fluids may become trapped in the pits of a rough pore surface forming an immiscible two-phase fluid interface with the invading fluid, allowing apparent slip flow at this interface. We present a two-phase fluid dynamics model, including interfacial tension, to characterize the impact of mineral surface roughness on this slip flow. We show that the slip flow can be cast in more familiar terms as a contact-angle (wettability) dependent effective permeability to the invading fluid, a non-dimensional measurement which relates the interfacial slip to the pore geometry. The analysis shows the surface roughness induced slip flow can effectively increase or decrease this effective permeability, depending on the wettability and roughness of the mineral surfaces. Configurations of the pore geometry where interfacial slip has a tangible influence on permeability have been identified. The results suggest that for large roughness features, permeability to CO_2 may be enhanced by approximately 30% during drainage, while the permeability to brine during re-imbibition may be enhanced or diminished by 60%, depending on the contact angle with the mineral surfaces and degrees of roughness. For smaller roughness features, the changes in permeability through interfacial slip are small. A much larger range of effective permeabilities are suggested for general fluid pairs and contact angles, including occlusion of the pore by the trapped phase.

1 Introduction

The influence of interfacial slip flow on rough, hydrophobic surfaces has been extensively studied in the field of microfluidics [*Steinberger et al.*, 2007; *Hyväluoma and Harting*, 2008; *Davis and Lauga*, 2009], whereby the flow will slip along the immiscible interface formed between the invading fluid and the fluid trapped in the roughness features of the surface. Fluid slip on these rough surfaces plays a key role in the engineering of superhydrophobic solid surfaces for industrial and consumer applications [*Rothstein*, 2010; *Song and Rojas*, 2013], where the flow can experience significant slip when transitioning from a Wenzel state [*Wenzel*, 1936] to a Cassie-Baxter state [*Cassie and Baxter*, 1944] where the surface roughness is quite pronounced (surface roughness features on the order of the pore length scale). Experimental, numerical and theoretical studies [*Steinberger et al.*, 2007; *Hyväluoma and Harting*, 2008; *Davis and Lauga*, 2009] have shown that depending on the protrusion angle that exists on the two-phase interface between the trapped and invading fluids, the flow may actually exhibit negative slip (increased flow resistance). It stands to reason that flow slip may occur in two-phase flows through geologic media and may impact the apparent permeability to fluid migration.

In this work we investigate the influence of interfacial slip on the calculation of effective phase permeability when residual fluid is trapped in roughness features on the walls of an individual rock pore. While our motivation is to investigate flows relevant to geologic carbon storage (GCS) (i.e. imbibition and drainage of supercritical CO_2 ($scCO_2$) and brine), the study also applies in general to two-phase flow of any immiscible fluids in porous materials (e.g., oil recovery, groundwater, geothermal energy, environmental remediation). In GCS, migration and capillary trapping of $scCO_2$ ganglia is strongly dependent on the contact angle of fluids on mineral grain surfaces [*Wang et al.*, 2012; *Chaudhary et al.*, 2013], and the contact angle depends on mineral surface wettability and roughness [*Chaudhary et al.*, 2015]. While formation permeability to migration of these ganglia depends mainly on characteristic pore body and throat dimensions, the impact of surface roughness on permeability through interfacial slip in a single pore has not been investigated in this context.

Injection of CO_2 in GCS perturbs the subsurface system, placing it in a state of mechanical and chemical disequilibrium. Aqueous CO_2 (CO_2 dissolved in resident brines) introduced during GCS may chemically react with formation rocks inducing mineral precipitation and dissolution [*Marini*, 2006] which can impact pore-scale fluid dynamics. Dissolution

processes create pits on mineral surfaces (i.e. dissolution "pitting") if the mineral becomes under-saturated with pore water, and has been extensively studied and documented for soils and sediments [*MacInnis and Brantley*, 1993]. Alternatively, mineral precipitation processes usually generate nanoparticles that may form thin coating films on mineral surfaces, which can substantially modify the surface properties of mineral grains and therefore the transport properties of geologic media at large [*Wang*, 2014]. These processes often happen simultaneously. It is well known that surface roughness affects surface wettability [*Wenzel*, 1936; *Cassie and Baxter*, 1944; *Herminghaus*, 2000] and can induce apparent slip flow along the rough surface [*Hyväluoma and Harting*, 2008; *Rothstein*, 2010]. Therefore, natural and reaction-induced surface roughness on mineral grains in reservoir rocks can alter the apparent contact angle along a wetting line, impacting wettability, and the apparent permeability of the reservoir rocks by introducing slip flow.

Roughness features on pore-walls in sandstones and shales have been measured using electron microscopes and characterized using fractal theory, which describes the degree of roughness of a given surface in terms of a fractal dimension [*Mandelbrot*, 1983; *Rys and Waldvogel*, 1986; *Korvin*, 1992; *Dimri*, 2005], which is a fraction lying between the topological and the Euclidian dimensions [*Brown and Scholz*, 1985]. The closer the fractal dimension is to the Euclidian dimension, the smaller the roughness features. The fractal dimensions reported for the pore spaces in sandstones [*Krohn*, 1988; *Schlueter et al.*, 1997] and shales *Wong et al.* [1986]; *Vallejo et al.* [2001] are closer to the Euclidian dimension for one-dimensional and two-dimensional measurements, which indicates that the roughness features are typically quite small compared to the average pore radii, which range from $0.01 - 1\mu\mathrm{m}$ for shales and $1 - 100\mu\mathrm{m}$ for sandstones [*Bobko and Ulm*, 2008; *Nelson*, 2009; *Elgmati et al.*, 2011]. The self-similar behavior of surface topography at different measurement scales has also been investigated, where the root-mean-squared roughness depths for various siltstone rock surfaces were measured and found to be $1000\times$ smaller than the measurement scale [*Brown and Scholz*, 1985]. Thus the effects on permeability from surface roughness should also be quite small in general [*Schlueter et al.*, 1997]. However, using confocal laser scanning microscopy, *Lieu* [2014] showed quite pronounced roughness features within micropores of sandstone specimens filled with clay particles, with roughness profiles that appear to have characteristic length scales on the order of the pore radius. *Schmatz et al.* [2015] using scanning electron microscopy in sandstone also shows images of large surface roughness features, created by kaolinite coatings, in quartz micropores of shales. This suggests that pore-wall surface roughness with features near the size of the pore-space is possible (although unusual) through the deposition and formation of secondary minerals in the larger pores. In these cases, the interfacial slip between the invading fluid and the trapped residual fluid pinned at these local heterogeneities [*Schmatz et al.*, 2015; *Brady et al.*, 2015] may have a non-negligible effect on the *local* effective phase permeability in the pore space.

Constructing a high-fidelity geometrical model of surface roughness, mimicking natural rough surfaces, is an intractable computational problem. It can be solved only approximately. We study the possible impact of roughness and wettability using a highly idealized geometrical model, as depicted in figure 1, wherein the hydrodynamic effect of roughness is modeled by a periodic arrangement of rectangular pits. While fully recognizing the idealized nature of this model, it does allow us to consider the essential physical nature of two-phase flow with surface tension in a pore with surface roughness scaled to the dimension of the pore. Although the model cannot well-represent the interstitial region of a porous rock, we believe it will yield physics-based estimates and scales for impact of roughness for given contact angles, fluid pairs and their viscosity ratio.

The impact of surface roughness in two-phase flow is manifested when the resident phase is trapped in roughness pockets as depicted in figure 1. As we shall see below, our theoretical model implies the roughness may allow slip flow which modifies effective permeability to the invading phase and will impact ganglion migration. Figure 2 depicts various fluid pair configurations that were considered, including trapped wetting fluid (figures 2(a,b)), and

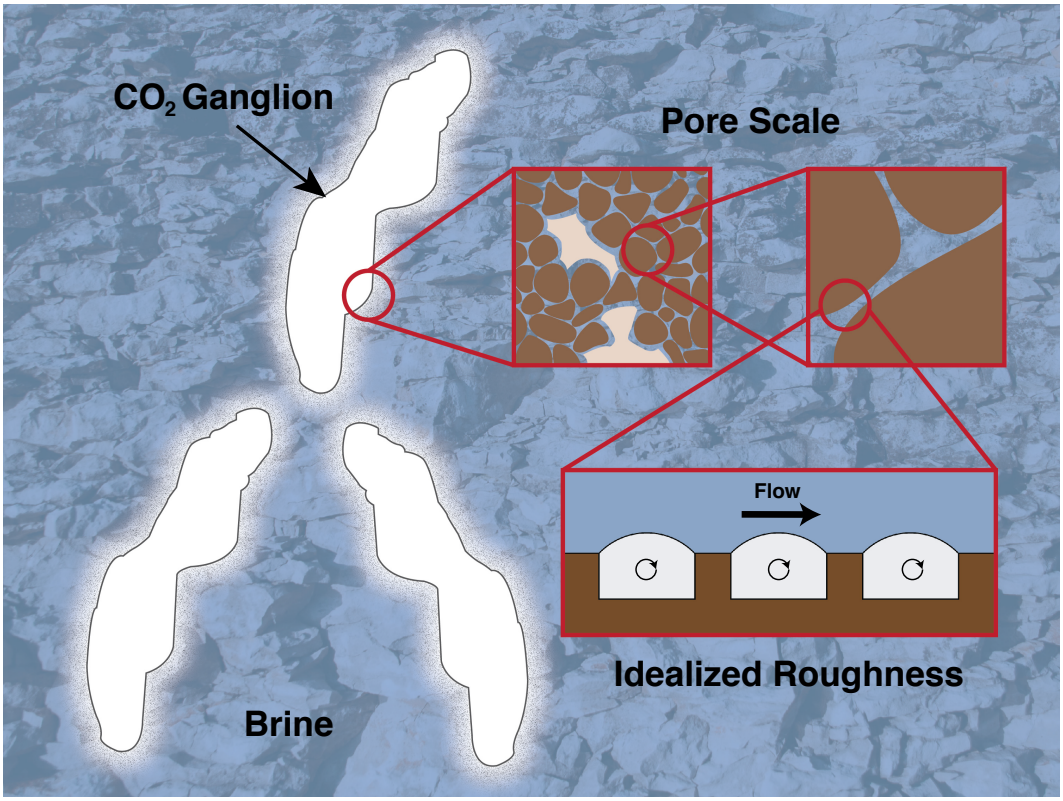

Figure 1. Conceptual roughness model relating the scales of $scCO_2$-brine ganglion dynamics to Cassie-Baxter theory. Here buoyantly-driven $scCO_2$ ganglion propagate through a reservoir initially saturated with brine, where brine or $scCO_2$ may become trapped in surface roughness features in the individual pores of the reservoir.

trapped nonwetting fluid (figure 2(d)), which could occur during imbibition in complex pore topology, as observed computationally [*Reddy et al.*, 2005]. Typically, immiscible two-phase displacement of a wetting fluid by a non-wetting fluid in geologic media leaves behind a sizable fraction of wetting fluid as residual saturation, in the form of films, trapped blobs and clusters [*Lake*, 1989; *Iglauer et al.*, 2011]. For GCS, the CO_2-brine system is slightly mutually soluble [*Duan and Sun*, 2003; *Spycher et al.*, 2003], and given sufficient time the residual films of brine slowly dissolve into the invading anhydrous CO_2 (figure 2(a)), leaving trapped pockets of brine in the surface roughness (figure 2(b)). However, continued dissolution of brine into dry CO_2 can result in formation "dryout" [*Pruess and Müller*, 2009; *Kim et al.*, 2012a] wherein roughness pockets are largely filled with supercritical CO_2 (figure 2(c)), except possibly for molecular films on minerals held by disjoining pressures [*Derjaguin*, 1955; *Radke et al.*, 1992] and capillary condensation effects [*Thomson*, 1872; *Tuller et al.*, 1999]. Adsorbedd films are not considered in the model.

Imbibition of brine into previously dried-out regions containing CO_2 can leave behind CO_2 trapped in the roughness pockets (figure 2(d)), owing to the complex topology of geologic pore space, as shown by numerical simulation [*Reddy et al.*, 2005], due to heterogeneous wettability or simply by capillarity. Capillary-induced surface energy minimization can lead to extreme local thinning of wetting films on wetting substrates as in the beading of an annular film of spider silk fluid on a spider web [*Goren*, 1962] and formation of fluid collars from a wetting film on the inside of capillary tube [*Hammond*, 1983]. This hydrodynamic configuration may promote flow slip and enhance (or hinder) apparent permeability to the re-

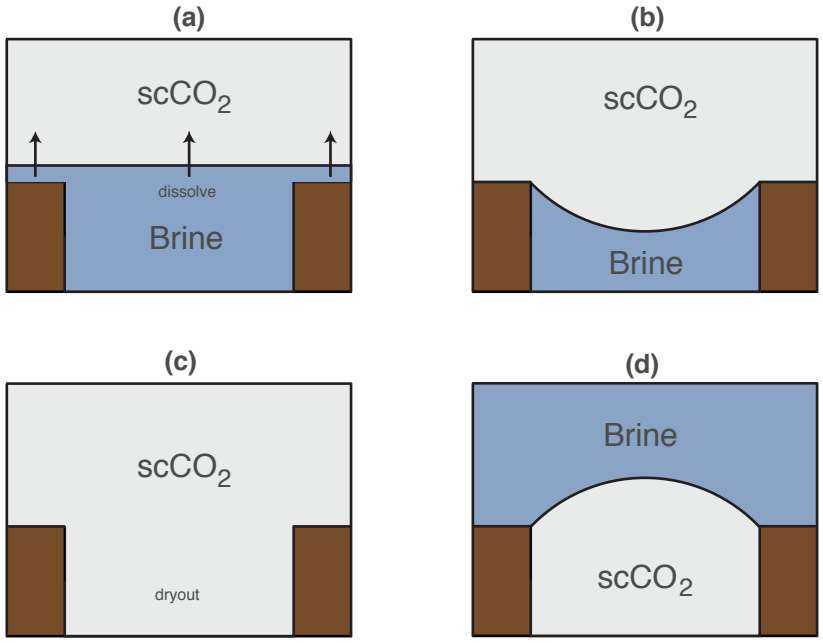

Figure 2. Description of the various Cassie-Baxter configurations (a) Brine film dissolving into $scCO_2$ ganglia during drainage, (b) Trapped brine in the surface roughness after brine is dissolved into $scCO_2$, (c) Configuration after "dryout" whereby the trapped brine has completely dissolved into the $scCO_2$ ganglia, (d) Configuration of trapped non-wetting $scCO_2$ after re-imbibition of brine at aft-end of $scCO_2$ ganglia.

imbibition of brine into the pore space. As a largely non-wetting fluid, the trapped CO_2 can block pore channels, contributing to capillary trapping of CO_2. Ultimately, the trapped CO_2 may dissolve into the brine thereby enhancing its density and possibly inducing buoyantly driven dissolution currents [*Martinez and Hesse*, 2016] assisting the upward buoyant flow of CO_2.

In addition to mechanisms associated with fluid phase dissolution, some injection reservoirs may not be strongly water-wetting, increasing the likelihood of CO_2 trapping in roughness pockets. Several recent core-flood experiments in intermediate-wet or oil-wet sandstone [*Iglauer et al.*, 2016; *Al-Menhali and Krevor*, 2016; *Rahman et al.*, 2016] have shown reduced oil or CO_2 residual saturation, with residual cluster shapes indicating wetting of smaller pores, hence higher likelihood of trapping in surface roughness. While CO_2 is typically considered non-wetting relative to brine, several studies have reported materials and conditions where CO_2 may intermediately wet the mineral surface. Sandstones are generally water-wet [*Lake*, 1989] however, the presence of clay or sorbed asphaltenes renders them mixed-wet or CO_2-wet [*Broseta et al.*, 2012; *Iglauer et al.*, 2011]. Carbonate reservoirs rich in organic material are generally oil-wet [*Treiber et al.*, 1972; *Chaudhary et al.*, 2013]. Some studies have noted that oil-wet media are often also CO_2-wet at reservoir conditions [*Broseta et al.*, 2012; *Chalbaud et al.*, 2009; *Iglauer et al.*, 2015; *Espinoza and Santamarina*, 2010; *Krevor et al.*, 2012; *Rahman et al.*, 2016]. For example in brine-CO_2 systems, the contact angle of the brine was reported to increase with pressure [*Broseta et al.*, 2012; *Chiquet et al.*, 2007; *Iglauer et al.*, 2014; *Jung and Wan*, 2012], or through geochemical reaction [*Kim et al.*, 2012b]. *Iglauer et al.* [2015] argue that for intermediate-wet rock, the complex interplay of pore morphology and wettability allows for both spontaneous and forced saturation changes. Owing to these complexities, this may lead to trapping of CO_2 in the surface roughness when the mineral surface is mixed-wet or CO_2-wet, analogous to the observations of entrapped air micro-bubbles on hydrophobic, air-wetting materials [*Rothstein*, 2010], where the flow is observed to slip

along the immiscible interface formed between the trapped (residual) phase and the invading non-wetting phase.

In the following we present a two-phase fluid dynamics model which solves the incompressible Navier-Stokes equation, including interfacial curvature, surface tension, and contact angle together with a simplified conceptualization of surface roughness to investigate the possible impact of surface roughness on ganglion migration for GCS. Injection of $\mathrm{scCO_2}$ into a brine-saturated reservoir alternately involves drainage (injection) and imbibition (buoyantly-driven $\mathrm{CO_2}$ migration), wherein brine or $\mathrm{scCO_2}$ may become trapped in the heterogeneous rough surfaces of mineral grains by the mechanisms discussed in the foregoing paragraphs. The next section describes this two-phase model and surface roughness concept. In the results section, we first define a new relationship between slip and effective permeability, based on our model concept. We then present general model results, for arbitrary fluid pairs and wetting behavior to illustrate how slip (effective permeability) depends on surface roughness in micropores, the contact angles of the trapped and injected fluid interfaces, and the viscosity of the working fluids. We then look at specific cases relating to the mobility of $\mathrm{scCO_2}$ ganglia in brine to gain an understanding of how the effects of surface roughness may impact ganglion dynamics in GCS systems (Section 3.2)

2 Computational model

2.1 Geometry

The conceptual model describing mineral roughness is shown in figure 1. Here, a pore in a porous geologic material is idealized as a two-dimensional channel with periodically spaced pits, representing natural or reaction-induced dissolution (or precipitation) pockets. Figure 3 shows a unit cell of such an idealized pitted channel with a periodic flow along the streamwise (x) direction, and having a characteristic total length (L) and characteristic channel half-height (h), which can be interpreted as the pore radius. The unit cell includes one "roughness pit" of length (λ) and depth (d). This geometry serves as an idealized, homogenized model of a real reservoir pore that may contain several repeating, heterogeneous roughness pits. The geometrical features of the roughness pits can be characterized by the dimensionless roughness parameter ($\beta = d/h$) and dimensionless pit-spacing parameter ($\varphi = \lambda/L$). The roughness parameter (β) relates the pit depth relative to the pore radius and provides a measure of the roughness in the rock. The geometry depicted in figure 3 is not necessarily typical, but is used to illustrate the geometry used in the subsequent results. Similarly, φ describes a relative measure of a characteristic wavelength of the roughness pits, and can be obtained from surface roughness measurements in a pore. Two immiscible fluids are present in this configuration; an injected fluid (Ω_{I}) with viscosity (μ_{I}) and density (ρ_{I}) and a trapped fluid (Ω_{T}) with viscosity (μ_{T}) and density (ρ_{T}) which resides in the roughness pit. Because these two fluids are assumed immiscible, they are separated by a two-phase fluid interface with a specified surface tension (γ) and wetting angle (θ) which is always referred relative to the trapped fluid phase. In addition to the roughness characteristics, this flow problem is characterized by the dimensionless viscosity ratio $\mu_{\mathrm{R}} = \mu_{\mathrm{I}}/\mu_{\mathrm{T}}$ and capillary number $\mathrm{Ca} = \mu_I \overline{u}/\gamma$, where $\overline{u}$ is the y-averaged streamwise velocity. The capillary number measures the importance of viscous forces to surface tension forces.

2.2 Fluid dynamics

The time-dependent, two-dimensional incompressible Navier-Stokes (NS) equation

$$\nabla \cdot \mathbf{u} = 0 \tag{1a}$$

$$\rho(\mathbf{x}) \left(\frac{\partial \mathbf{u}}{\partial t} + (\mathbf{u} \cdot \nabla)\, \mathbf{u} \right) = -\nabla p + \nabla \cdot \left(\mu(\mathbf{x}) \left(\nabla \mathbf{u} + \nabla \mathbf{u}^{\mathrm{T}} \right) \right) \tag{1b}$$

is used to model the fluid flow between immiscible fluids in the pore. Equations 1a and 1b are solved in the physical domain Ω, where $\mathbf{x} \in \Omega$, $\mathbf{u} = \langle u, v \rangle$ is the velocity vector, and p is the

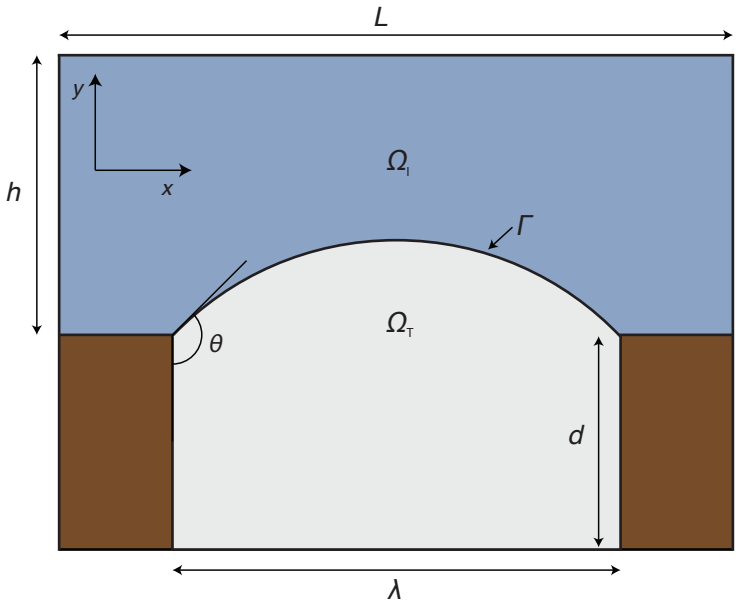

Figure 3. Geometry of the two-phase, streamwise periodic unit cell of a "roughness pit".

pressure. The density $\rho(\mathbf{x})$ and viscosity $\mu(\mathbf{x})$ are expressed as function of $\mathbf{x}$ and are assigned locally either in the injected domain $\Omega_{\mathrm{I}} \subset \Omega$ or the trapped domain $\Omega_{\mathrm{T}} \subset \Omega$, separated by the interface Γ. The fluids are immiscible and a constant surface tension γ is exerted along their common interface. The boundary conditions on Γ are

$$[\mathbf{u}]_{\Delta} = 0, \qquad \mathbf{x} \in \Gamma \tag{2a}$$

$$[-p\mathbf{I} + \mu(\mathbf{x})\left(\nabla\mathbf{u} + \nabla\mathbf{u}^{\mathrm{T}}\right)]_{\Delta} \cdot \hat{\mathbf{n}} = -\gamma\kappa\hat{\mathbf{n}}, \qquad \mathbf{x} \in \Gamma \tag{2b}$$

where $\hat{\mathbf{n}}$ is the surface normal on Γ, κ is the interface curvature, and $[\cdot]_{\Delta}$ represents a jump of the bracketed expression across the interface. The interface (Γ) is a material surface on which the velocity is continuous (equation 2a) and the stresses are discontinuous in the normal direction by an amount proportional to the surface curvature, as expressed by equation 2b. In the absence of viscous stresses, this equation reverts to the familiar balance between the capillary pressure and surface tension across a curved interface. The no-slip condition is employed on all solid surfaces and a sheer-free boundary condition is imposed at the top boundary to ensure symmetry across the principle flow axis (x). Finally, periodic boundary conditions are enforced in the streamwise (x) direction and the flow is driven by a pressure gradient in that direction, to be detailed in the next section.

The Navier-Stokes equation (equations 1a and 1b) is solved subject to the boundary conditions (equations 2a and 2b) using a moving mesh Arbitrary Lagrangian Eulerian (ALE) finite element method implemented in the multimechanics module of the Sierra code suite [*Notz et al.*, 2007]. The equations are discretized using the Galerkin Finite Element Method (FEM). Linear basis functions are used for the continuity, momentum, and mesh equations on unstructured triangular elements. In general, the edge length of an element is no more than $\Delta_{\mathrm{E}} = 0.03h$, which provides grid independent solutions. Scaling our mesh size to the geometry keeps our solutions grid independent when scaling to higher roughness and pit-spacing parameters, although it does increase the problem size. The pressure-stabilizing/Petrov-Galerkin (PSPG) method is used to provide stable solutions with equal order elements for pressure and velocity.

The mesh is deformed using a pseudo-solid equation subject to a kinematic condition on the interface between the fluids [*Cairncross et al.*, 2000]. The motion of the pseudo-solid

on the interior is governed by the quasi-static equation

$$\nabla \cdot \mathbf{S} = 0 \tag{3}$$

where $\mathbf{S}$ is the pseudo-solid stress given by

$$\mathbf{S} = \lambda e \mathbf{I} + 2\mu \mathbf{E} \tag{4}$$

where λ and μ are the Lame constants (here both arbitrarily set to 1000), e is the volume strain, and $\mathbf{E}$ is the small strain tensor given by

$$\mathbf{E} = \frac{1}{2}\left[\nabla \mathbf{d} + \nabla \mathbf{d}^T\right] \tag{5}$$

where $\mathbf{d}$ is the mesh displacement. This simple model is adequate for the current work because the displacements are small. The kinematic condition ties the mesh displacement at the fluid interface to the normal velocity at the interface. The resulting boundary condition on Γ is

$$(\mathbf{u} - \dot{\mathbf{d}}) \cdot \hat{\mathbf{n}} = 0, \qquad \mathbf{x} \in \Gamma \tag{6}$$

where $\dot{\mathbf{d}}$ is the time derivative of the mesh displacement. This is a scalar condition that is to be applied to the normal mesh displacement. To accomplish this, the pseudo-solid equations are rotated from Cartesian coordinates into a normal-tangent coordinate system. After rotating the equations, the row of the equations associated with the normal direction is replaced with the kinematic condition in equation 6.

The resulting nonlinear, fully-coupled monolithic system (a system in which the velocity, pressure, and mesh displacement degrees of freedom are solved simultaneously) is solved using the iterative Newton method. The resulting linear system of equations are solved using the generalized minimum residual method (GMRES) with incomplete LU decomposition (ILU) using the Trilinos [*Heroux et al.*, 2003] library. For a detailed formulation of the numerical method, including the derivation of the Galerkin Finite Element method and the ALE method used in the present simulations, please refer to *Cairncross et al.* [2000].

The ALE method is used here as the mesh deformation is expected to be quite small (the fluid/fluid interface is nearly static), and thus we solve the velocity, pressure, and mesh motion simultaneously in the same nonlinear system. Due to the monolithic nature of the present numerical method, no spurious currents commonly observed in segregated interface tracking algorithms exist [*Hysing*, 2006]. The results presented in the subsequent sections are solved direct to steady state, as capturing the dynamic evolution of these capillary systems is not required for the calculation of the final, steady-state interface slip. Therefore, all results presented are the final steady state solutions.

2.3 Case descriptions

In all cases, the capillary number was held as a constant $\mathrm{Ca} = 1 \times 10^{-7}$, which corresponds to slow flows dominated by capillary forces. Such flows are driven by a small imbalance (quasi-equilibrium) between capillary and buoyant forces, conditions which are anticipated to prevail at long times after injection in GCS applications [*Meckel et al.*, 2015]. An investigation consisting of various fluid pairings and geometrical configurations is made in the subsequent sections. In order to keep Ca constant for different geometrical configurations, the applied mean pressure gradient is prescribed as

$$\frac{\mathrm{d}\overline{p}}{\mathrm{d}x} = \frac{12\gamma \mathrm{Ca}}{h^2} \tag{7}$$

for all simulations. The aim of this study is to investigate, in particular, two-phase systems containing brine and $\mathrm{scCO_2}$. Therefore, for all simulations, the interfacial surface tension was held as a constant at the value $\gamma = 0.035$ N/m [*Bennion and Bachu*, 2006]. However, in order to extend the generality of this study, the fluid pairings will exhibit a range in viscosities such

that $1 \times 10^{-3} \leq \mu_{\mathrm{R}} \leq 1 \times 10^{4}$ which encompasses a wide range of applications in the context of multiphase flow in reservoirs. Similarly, a large range in both the geometric parameters β and φ will be selected in order to elucidate the effective limits of the reservoir rock geometry on the slip length and the permeability of the reservoir. In other words, we aim to determine at what relevant length scales does interfacial slip influence the permeability characteristics of the pore, and is discussed in section 3.1.2.

The angle θ made between the two-phase fluid interface and pit corner relative to the trapped fluid will be referred to as the "wetting angle" and is referenced in figure 3. This wetting angle is enforced as an initial condition by placing a circle of appropriate radius to fit the required pit length λ at the desired wetting angle θ. This wetting angle will span the range $0^{\circ} \leq \theta \leq 180^{\circ}$ to fully capture the possible range of wetting configurations of the trapped fluid, whereby the trapped fluid is either in a "wetting" ($\theta < 90^{\circ}$) or "non-wetting" ($\theta > 90^{\circ}$) state. In all simulations, the trapped fluid is pinned at the corners (an assumption which can be made at low capillary numbers) and a no-slip condition ($\mathbf{u} = \mathbf{0}$) is enforced on all solid interfaces (brown surfaces in figure 3). Sweeping through a large range of these various geometric and fluid quantities will ensure the applicability of these results to a wide range of fluid pairings and geometric attributes commonly observed in GCS and other reservoir flows (i.e. natural gas extraction, enhanced oil recovery, etc.) as well as for geometries in microfluidics. For results and parameters related directly to GCS, please refer to section 3.2.

3 Results and discussion

In fluid mechanics, the no-slip boundary condition implies that the fluid velocity at the fluid-solid interface is equal to the velocity of the solid surface and is generally valid in large-scale, macroscopic flows. However, at microscopic scales, this assumption is often not valid [*de Gennes et al.*, 2004]. Fluid slip can be calculated by introducing a slip velocity on a wall, defined as $u_{\mathrm{w}} = b|\partial u/\partial y|_{\mathrm{w}}$. Here, b is the slip length and is defined as the distance below the solid surface where the velocity linearly extrapolates to zero. For this study, it is useful to characterize the slip in terms of an effective permeability to flow. In a two-dimensional, pressure-driven channel that can exhibit slip on the walls, the permeability K_{S} can be calculated from the analytic solution of the velocity profile $\langle v(y) \rangle$ for 1D plane-Poisiuelle flow whereby one wall may exhibit slip (u_{w}). Using the average $\langle v(y) \rangle$ channel velocity, the permeability can be expressed through the relationship $K = \mu \langle v(y) \rangle \mathrm{d}p/\mathrm{d}x$, which yields

$$K_{\mathrm{S}} = \frac{h^2}{4}\left(\frac{1}{3} + \frac{b}{b+h}\right) \tag{8}$$

where b is the slip length and h is the pore width. When the slip length $b = 0$, the permeability of plane-Poisiuelle flow is recovered ($K_{\mathrm{NS}} = h^2/12$). Therefore, the permeability of the channel can be classified as either no-slip (K_{NS}) when $b = 0$ or, if one wall exhibits slip ($b \neq 0$), as K_{S}. Using these classifications, the effective permeability K_{E} can be defined as

$$K_{\mathrm{E}} = \frac{K_{\mathrm{S}}}{K_{\mathrm{NS}}} = 1 + \frac{3b}{b+h} \tag{9}$$

and is a non-dimensional quantity whose value is calculated relative to a given pore geometry. Based on this equation, if the slip length $b = 0$, the effective permeability $K_{\mathrm{E}} = 1$. Similarly, if the slip length is negative ($b < 0$) then $K_{\mathrm{E}} < 1$ and the channel is *less* permeable compared to a pore with no roughness. Similarly, if the slip length is positive ($b > 0$) then $K_{\mathrm{E}} > 1$ and the channel is *more* permeable. From equation 9, K_{NS} can also be recovered if the slip length is much smaller than the characteristic pore radius ($b \ll h$). Therefore K_{E} essentially provides a measure to the *relative* importance of slip in the context of the local flow field permeability based on the characteristic geometric features of the reservoir.

The slip length is calculated from the numerical solution of the two-phase problem described in the previous section. The effective permeability is the ratio of volumetric flow rate obtained from the solution of the two-phase problem to the flow rate of invading fluid in the

absence of the roughness pit, both subject to the same pressure gradient described in equation 7. Thus, the resulting effective permeability and slip length depend on the contact angle, viscosity ratio, and surface roughness characteristics and are measured directly from the resulting calculated volumetric flow rate from the two-phase flow calculation. This contact-angle-dependent effective permeability K_{E} to the invading fluid is applicable at residual saturations of the resident fluid.

3.1 Slip-enhanced effective permeability of rough channels for arbitrary fluids

In this section we investigate the influence of both wetting configurations and roughness geometry on permeability for pairs of arbitrary fluids in arbitrary geometries. The fluids are chosen arbitrarily in the sense that their wetting configurations are independent of their viscosity ratios so that these results can be applied in a more general sense. This allows us to gain fundamental physical insight on how all possible permutations of viscosity ratio, geometry, and wetting configurations can affect the permeability of a narrow, rough microchannel. In the next section we will investigate these results applied to a $\mathrm{scCO_2}$-brine system where certain configurations presented here will be invalid based on the dependence of wettability and viscosity ratio for this particular system.

3.1.1 Influence of wetting configurations

The effective permeability (K_{E}) for a range of viscosity ratios (μ_{R}) and wetting angles (θ) is displayed in figure 4, where the geometry for these simulations is fixed ($\varphi = 0.63$ and $\beta = 1$) in order to isolate the effect of fluid pairings and wetting configurations on the flow field permeability. This geometry was chosen to emphasize the effect of interfacial slip on sufficiently rough pores and to isolate the effect of wetting configurations and viscosity ratio on permeability. The influence of geometry is discussed in section 3.1.2. For a high viscosity ratio $\mu_{\mathrm{R}} = 1 \times 10^4$ (e.g. invading water, trapped air), agreement with previous studies on entrapped air microbubbles is good [*Steinberger et al.*, 2007; *Hyväluoma and Harting*, 2008; *Davis and Lauga*, 2009] whereby a local maxima in fluid slip occurs for protruding bubbles ($\theta > 90^\circ$), and therefore serves to validate our treatment of the two-phase interface used in these computations. In particular, the current reported value of the no-slip ($K_{\mathrm{E}} = 1$, $b = 0$) contact angle $\theta \approx 148^\circ$ is in excellent agreement with the value reported by *Steinberger et al.* [2007] which reports $\theta \approx 152^\circ$ (converted to our definition of θ).

For flows with high viscosity ratios, the trapped fluid is relatively inviscid to the injected fluid and in general slip flow ($K_{\mathrm{E}} > 1$) is observed for a wide range of wetting angles. In this case, the relatively inviscid trapped fluid will reduce friction on the wall (lubrication) thus increasing the volumetric flow in the channel at a fixed pressure gradient. In agreement with the aforementioned studies on microbubbles, maximum lubrication occurs when the relatively inviscid trapped fluid forms an angle $\theta \approx 100^\circ$ in a configuration such that the two-phase interface is slightly raised across the top of the pit and protrudes into the channel. The lubricating effect decreases with increasing wetting angles as the two-phase interface further protrudes into the channel, effecting a flow constriction with respect to the channel flow, thereby resulting in $K_{\mathrm{E}} < 1$ (and therefore $b < 0$), despite the fact that the trapped fluid is inviscid compared to the injected fluid. In general, for all viscosity ratios, there is a region in the range of θ where the flow is self-lubricating ($K_{\mathrm{E}} > 1$), and this region is extended as the viscosity ratio μ_{R} increases. Within this region, there exists a local maximum in K_{E} when $\mu_{\mathrm{R}} > 1$ ($\mu_{\mathrm{I}} > \mu_{\mathrm{T}}$) which is asymptotic in the limit as $\mu_{\mathrm{R}} \to \infty$ and is shown in the inset of figure 4. This local maximum can either increase or decrease depending on the roughness characteristics β and ϕ, which is detailed in the next section.

At the other extreme, when the trapped fluid is much more viscous than the flowing channel fluid ($\mu_{\mathrm{R}} = 1 \times 10^{-3}$), a lubricating condition is possible only for configurations in which the trapped fluid is in a wetting configuration ($\theta < 90^\circ$), where the meniscus recedes into the pit. Here the fluid interface effectively becomes the lower surface of the pit and

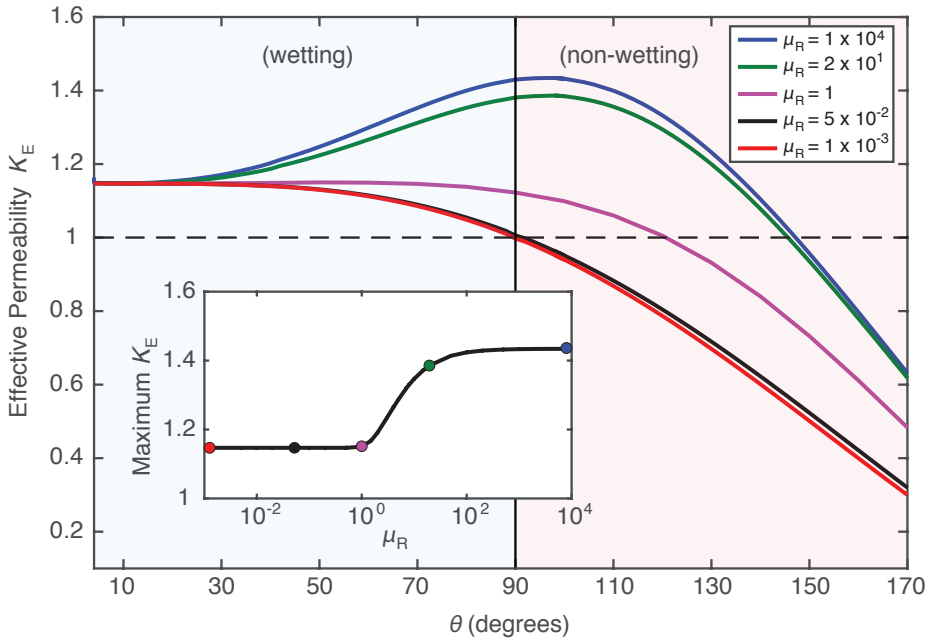

Figure 4. Effective permeabilities (K_{E}) as a function of wetting angle (θ) for different fluid viscosity ratios (μ_{R}) and fixed geometry ($\varphi = 0.63$ and $\beta = 1$); the the dashed-line represents the no-slip case where $K_{\mathrm{E}} = 1$. The inset displays the maximum effective permeabilities as a function of viscosity ratio (μ_{R}) where the colored circles represent the maximum K_{E} of the colored curves. The blue shaded and red shaded region represent wetting ($\theta < 90^\circ$) and non-wetting ($\theta > 90^\circ$) configurations, respectively.

the flowing fluid is self-lubricating. Notice that this self-lubricating effect is independent of viscosity ratio for $\theta < 30^\circ$, wherein the trapped fluid wets the pit. In this region, K_{E} is now a constant and its corresponding wetting angle $\theta \approx 0^\circ$, which corresponds closely to the Wenzel state [*Wenzel*, 1936] where the injected fluid wets the entirety of the pit. The rigid-wall solution ($K_{\mathrm{E}} = 1$) is recovered for neutral wetting configurations ($\theta = 90^\circ$), where the flat interface affects a no-slip condition. For increasing wetting angle the protruding interface reduces the permeability, ultimately decreasing to roughly 30% of the permeability of the pit-free channel. The curve for iso-viscous fluid pairs is similar to the curve for $\mu_R \to 0$ but with a larger region of contact angle in which $K_{\mathrm{E}} > 1$.

3.1.2 Impact of roughness geometry

Now we turn our attention to how the characteristics of surface roughness will modify the effective permeability of a two-phase flow for viscosity ratios where $\mu_{\mathrm{R}} > 1$ or $\mu_{\mathrm{R}} < 1$. These fluid pairs will have three extreme wetting configurations $\theta = 0^\circ$ (wetting), $\theta = 90^\circ$ (neutral), and $\theta = 180^\circ$ (non-wetting) and are, again, independent of the viscosity ratio for the two fluids. In this investigation, the surface roughness ($\beta = d/h$) and pit spacing ($\varphi = \lambda/L$) parameters will be varied independently with the other held as a constant in order to ascertain their functional dependence on permeability.

Figure 5(a) shows the dependency of the effective permeability K_{E} on the roughness ratio β. In this plot, $\varphi = 0.63$ and is held as a constant. As noted above, when $\theta = 0^\circ$ the meniscus recedes into the pit and the flow self-lubricates, and the permeability becomes independent of viscosity ratio. That is, the effective permeability of the reservoir becomes invariant to the properties of the working fluid pairs when the trapped fluid exhibits extreme

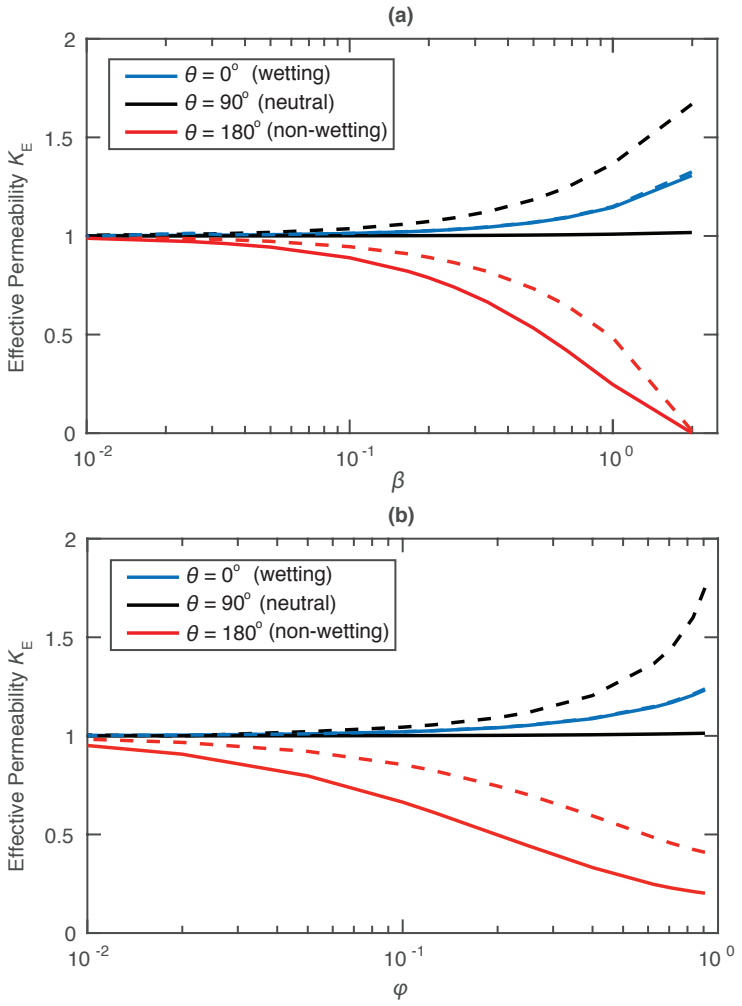

Figure 5. Effective permeabilities (K_{E}) as a function of (a) surface roughness (β); (b) roughness spacing (φ) at three trapped fluid wetting conditions (wetting, non-wetting, and neutral). Solid lines represent a system where $\mu_{\mathrm{R}} = 0.05$, dashed lines represent a system where $\mu_{\mathrm{R}} = 20$.

wetting conditions. However, in a case where the wettability is neutral ($\theta = 90°$), the behavior of the channel permeability is dictated by the viscosity of the working fluids. For $\mu_{\mathrm{R}} < 1$ the permeability is independent of the roughness parameter β due to the recovery of the rigid wall solution at $\theta = 90°$ (see figure 4). That is, the slip length $b \approx 0$ for this case which renders $K_{\mathrm{E}} = 1$ from equation 9 and is independent of the channel height h. However, when $\mu_{\mathrm{R}} > 1$, the dependency of K_{E} on β is recovered, and the flow is self lubricating to various degrees. In extreme non-wetting cases $\theta = 180°$, the protrusion of the two-phase interface acts to constrict the flow, greatly reducing the permeability of the system when $d \approx h$ and leads to capillary bridging across the pore space, enhancing capillary trapping phenomena. The permeability can be enhanced or diminished substantially when $d > 0.1h$.

The influence of the pit-spacing parameter φ on the effective permeability K_{E} can be observed in figure 5(b). The behavior is similar to that of the surface roughness parameter (β), in that the influence of the pit-spacing on the flow permeability becomes substantial as the length of the pit (λ) approaches the characteristic length of the pore (L). The impact of the roughness pits vanishes at large spacings ($\lambda \ll L$) and suggests that the pore must be adequately rough for the interface slip to affect the pore permeability. Otherwise, the impact

of wetting configuration and viscosity ratio is similar to the impact of roughness magnitude. We can conclude that the geometric characteristics of the pore play an important role in how the slip can influence the localized phase permeability. The surface roughness profiles, in which the appropriate β and φ terms can be obtained from experimental measurements, may effectively reduce or enhance the permeability of the pore and is mostly heavily dependent on the properties of the working fluids and wetting angle of the two-phase interface.

3.2 Slip-enhanced effective permeability of $scCO_2$-brine systems for GCS

During drainage, $scCO_2$ ganglia invades resident brines in the subsurface, eventually trapping brine in the roughness features (figure 2(b)). Prolonged flow of CO_2 ganglia through the pore space can result in formation dry-out, causing $scCO_2$ to become trapped in the roughness feature as discussed earlier and illustrated in figure 2(c). At the aft end of the ganglia, an imbibition process occurs as the resident brine wicks back into pore space vacated by buoyant CO_2, potentially trapping the CO_2 in the roughness pit as the brine imbibes into the pore space [*Reddy et al.*, 2005]. In each case, when the roughness-trapped fluid configuration is attained, the wettability of the trapped fluid ($scCO_2$ in imbibition, brine in drainage) will influence the shape of the two-phase interface and thus introduce a dependency on the wetting angle and on the viscosity ratio in figure 4.

For a drainage scenario, $scCO_2$ invades trapped brine ($\mu_R = 0.05$) and the brine will generally wet the rock (when considering sandstone or shale, for example) and thus yield a wetting angle in which $\theta < 90°$ (figure 2(b)). In an imbibition scenario, brine invades trapped $scCO_2$ ($\mu_R = 20$) and the trapped $scCO_2$ will be generally non-wetting and thus yield wetting angles such that $\theta > 90°$ (figure 2(d)). The permeability curves of these two configurations are illustrated in figure 6, in which only portions of the full permeability curves displayed in figure 4 are physically relevant. In a drainage scenario (blue curve in figure 6) the permeability is

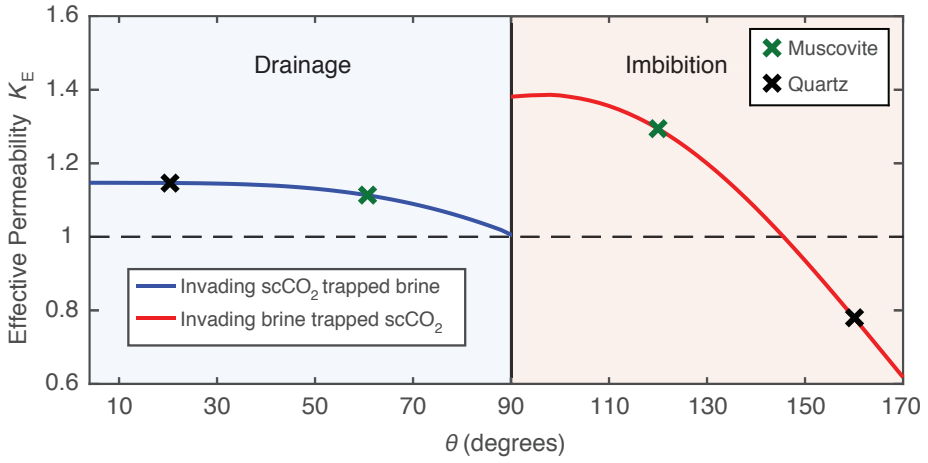

Figure 6. Effective permeabilities (K_E) as a function of wetting angle θ for a $scCO_2$-brine system undergoing imbibition and drainage processes in a fixed geometry ($\varphi = 0.63$ and $\beta = 1$). Marked crosses represent wetting configurations in which quartz or muscovite are the working minerals [*Chaudhary et al.*, 2015] which may be present in shales and sandstones.

always enhanced in the presence of surface roughness, and is independent of the wetting angle from $0° < \theta < 50°$. From $50° < \theta < 90°$, the brine is less wetting and the permeability is enhanced although to a lesser degree than in a more extreme wetting case. In this drainage configuration, the neutral wetting case ($\theta = 90°$) exhibits zero slip at the interface and the

permeability is unaffected by the surface roughness. However, in imbibition (red curve), the opposite is true for neutral wetting and the permeability is more enhanced compared to any drainage scenario, with a maximum permeability occurring at $\theta \approx 100°$. The most interesting feature of an imbibition scenario is that surface roughness can affect either an enhanced or diminished permeability depending on the wettability of the system, where the delineation occurs at $\theta = 146°$ (which we will deem the cross-over point). To emphasize this, green and black crosses have been marked in figure 6 that indicate two possible wetting conditions of a $\mathrm{scCO_2}$-brine system. The green mark represents a wetting configuration for a $\mathrm{scCO_2}$-brine system in muscovite or shale sample [*Chaudhary et al.*, 2015] where $\theta = 60°$ (relative to trapped brine). The black mark indicates a more extreme wetting condition that may exist in which $\theta = 20°$ (again relative to the brine) when the pore is composed of quartz (abundant in sandstones) [*Chaudhary et al.*, 2015]. In $\mathrm{scCO_2}$-brine imbibition, wetting configurations dictated by mineral composition can enhance or diminish the permeability characteristics of a rough pore and introduce a cross-over point in the effective permeability curve.

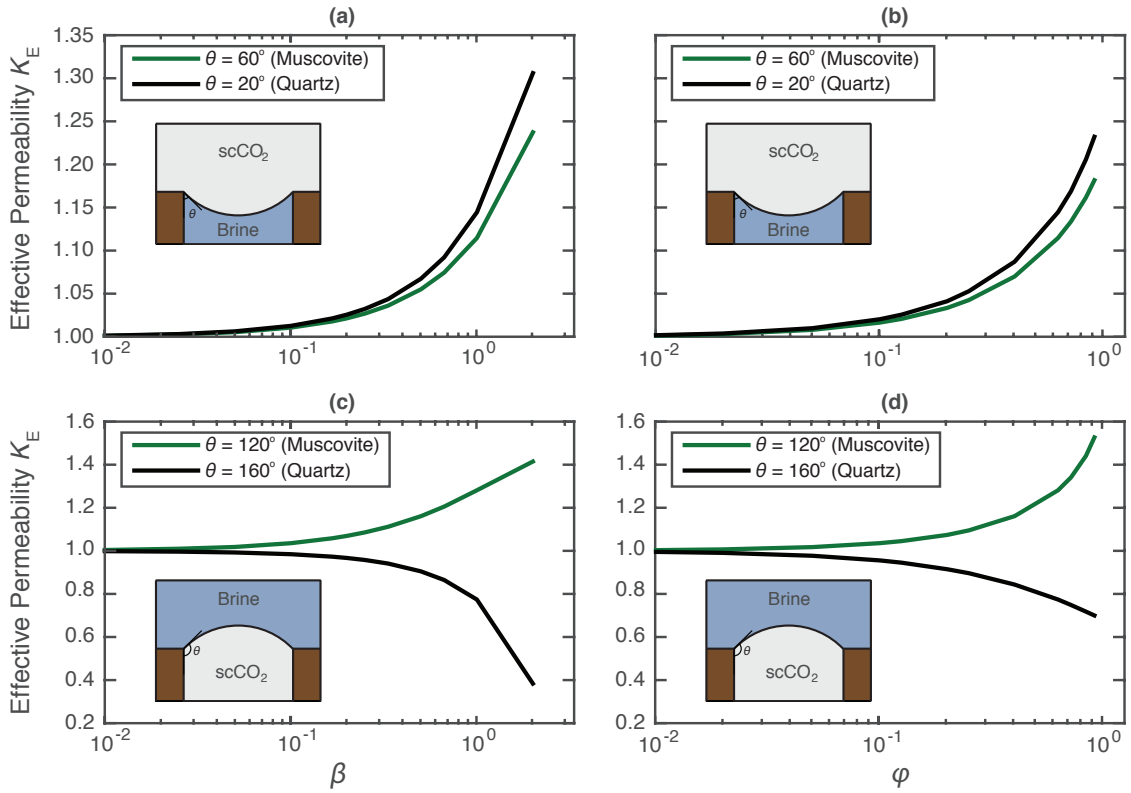

Figure 7. Effective permeabilities (K_{E}) as a function of surface roughness (β) and roughness spacing (φ) for muscovite and quartz minerals; (a,b) represents an $\mathrm{scCO_2}$-brine drainage scenario, (c,d) represents an $\mathrm{scCO_2}$-brine imibibition scenario.

Figure 7 shows the dependency of the permeability on the roughness ratio β and spacing parameter φ for the contact angles marked in figure 6. For a drainage scenario (figure 7(a,b)) both wetting configurations show enhanced permeability, with the more-wetting $\theta = 20°$ (quartz) exhibiting higher permeability enhancement for all β and φ. This is attributed to the increased convexity of the interface (which extends far down into the pit) as a result of the increased hydrophilicity of quartz compared to muscovite (see inset in figure 7(a,b)). In imbibition, however, the trapped $\mathrm{scCO_2}$ may either enhance or diminish permeability depending

on the wettability characteristics of the reservoir. For $\theta = 120°$, where the brine exhibits mixed wettability, the presence of trapped $\mathrm{scCO_2}$ enhances permeability for large roughness ratio (β) and spacing parameters (φ). This is the opposite for $\theta = 160°$ (quartz), where the brine is hydrophilic. In this case (black curve) the trapped $\mathrm{scCO_2}$ acts to constrict the flow in the pore-throat due to the extreme concavity of the $\mathrm{scCO_2}$-brine interface, contributing to $\mathrm{scCO_2}$ or brine trapping in the pore. It should be noted that there is extreme sensitivity of permeability enhancement or diminishment to the roughness ratio β, where $\beta > 0.1$ must be satisfied for any noticeable affect on permeability. As noted in the introduction, this degree of roughness appears to be rather uncommon and thus the influence of interfacial slip to enhance or diminish permeability within a single pore should be regarded as a secondary effect, although it's impact can be quite severe for very rough pores.

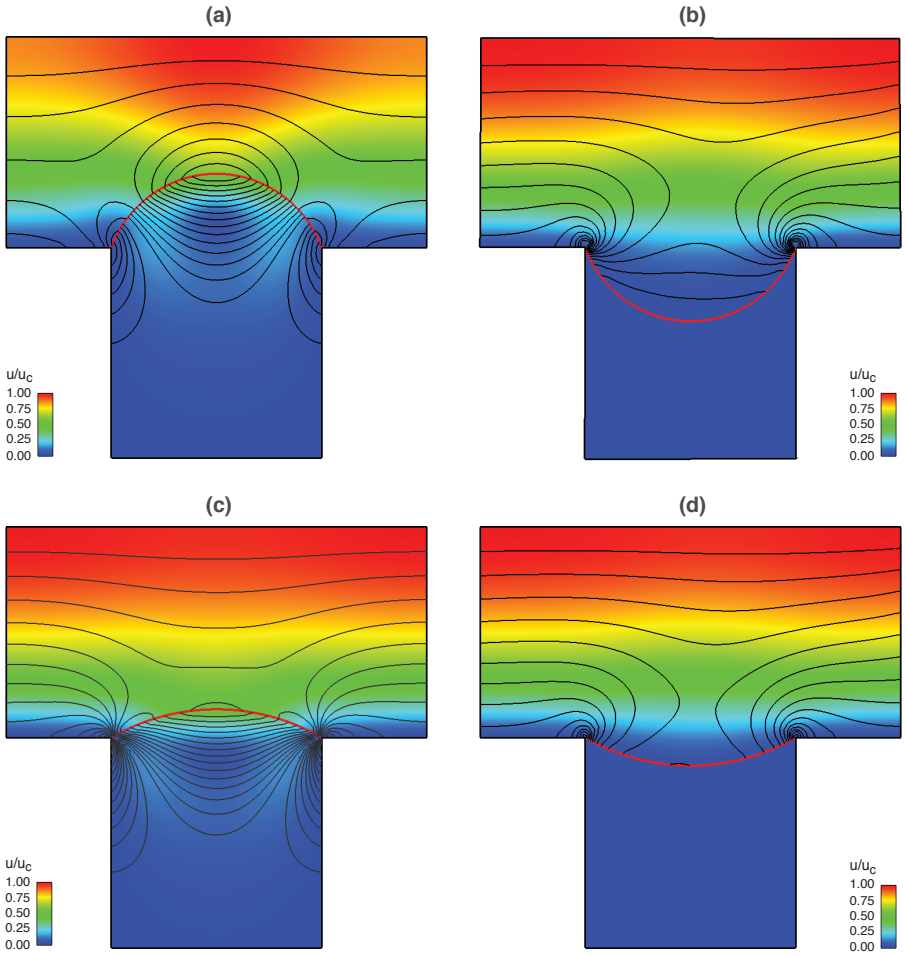

Figure 8. Steady-state solution colored by velocity magnitude (non-dimensionalized by the streamwise centerline velocity u_c with vorticity contours (black lines) super-imposed for (a) An imbibition configuration where $\theta = 160°$, $\mu_R = 20$ (invading brine, trapped $\mathrm{scCO_2}$), (b) A drainage configuration where $\theta = 20°$, $\mu_R = 0.05$ (invading $\mathrm{scCO_2}$, trapped brine), (c) An imbibition configuration where $\theta = 120°$, $\mu_R = 20$ (invading brine, trapped $\mathrm{scCO_2}$), (d) A drainage configuration where $\theta = 60°$, $\mu_R = 0.05$ (invading $\mathrm{scCO_2}$, trapped brine). For all four cases, $\beta = 1$ and $\varphi = 0.5$. The two-phase interface is colored red for clarity.

Figure 8 shows the final, steady-state solutions for imbibition and drainage scenarios highlighted in figure 6 (red and black marks). Here, the flow field is colored by velocity magnitude with contours of vorticity super-imposed on the color map. At this capillary number, $Ca = 1 \times 10^{-7}$, the interface remains static for all cases (see *Hyväluoma and Harting* [2008]). For the imbibition cases (figures 8(a,c)), significant rotation is observed at the top of the interface and near the center of the trapped phase. The rotation in the trapped phase is similar in nature to a flow in a driven-cavity at low Reynolds number [*Kim and Moin*, 1985]. This rotation is absent in the trapped phase for the drainage cases (figures 8(b,d)), owing to the fact that viscosity of the trapped brine is higher than the invading $\mathrm{scCO_2}$ phase. As discussed in section 3.1, the more viscous trapped fluid is "rigid" relative to the invading fluid, and therefore any permeability enhancement shown in figure 6 (blue curve) can be attributed to the fact that the interface recedes into the pit, providing higher flow rates and thus higher permeabilities when compared to a rigid, flat interface (i.e. a wall). As shown earlier in figure 6 (red curve), in imbibition cases the interface contact angle plays an important role in the enhancement or diminishment of the permeability. In the less non-wetting case ($\theta = 120^\circ$) shown in figure 8(c), higher velocity is maintained close to the interface and throughout the channel, compared to the more non-wetting case ($\theta = 160^\circ$) shown in figure 8(a). This implies that the volumetric flow rate, and thus the permeability, will overall be lower than that of the less non-wetting case (as confirmed in the calculation of K_E in figure 6).

4 Summary and Conclusions

In this study, an investigation was made to assess the influence of interfacial slip of phases trapped in pore-scale surface roughness features using CFD, building on previous studies involving the flow of water on entrapped air microbubbles [*Steinberger et al.*, 2007; *Hyväluoma and Harting*, 2008; *Davis and Lauga*, 2009] but applied to geophysical flows at low capillary number. A relationship between the slip length b and the effective permeability K_E was derived for a simple pressure-driven channel flow to assess the influence of interfacial slip that may occur due to the trapping of residual fluids in surface roughness features. The effective permeability provides a useful, non-dimensional measurement of the influence of interfacial slip compared to the characteristic length scale of the pore (in this case, the pore radius).

First, the influence of the interfacial contact angle for arbitrary fluid pairs and wetting configurations was assessed. In these more general cases (where β and φ are relatively large), it is shown that for trapped viscous fluids ($\mu_\mathrm{R} < 1$), the permeability is only weakly enhanced when the trapped fluid wets the pit ($\theta < 90^\circ$) and is nearly independent of the contact angle when $\theta \leq 40^\circ$ where there is approximately a 15% increase in the permeability. For non-wetting cases ($\theta > 90^\circ$) the permeability is diminished and is a strong function of the contact angle, yielding up to a 70% reduction in the permeability when $\theta \approx 170^\circ$. For less viscous trapped fluids ($\mu_\mathrm{R} > 1$), the pore permeability is enhanced in both wetting and non-wetting configurations, with a local maxima in K_E occurring at approximately $\theta \approx 100^\circ$ (a weakly non-wetting configuration). A viscosity-dependent cross-over point between enhanced and diminished permeability occurs for non-wetting configurations, which suggests a strong dependence on the wettability of the trapped fluid to either self-lubricate or trap the injected fluid. The pore geometry was varied systematically to identify surface roughness attributes where the interfacial slip had a tangible influence on the pore-scale permeability. For the arbitrary fluid pairs studied, it was concluded that for the interfacial slip to affect the effective permeability (either through enhancement or diminishment) the geometric roughness features must be sufficiently large with respect to the characteristic pore features (β and φ must be $\mathcal{O}(10^{-1})$ and larger).

The generalized results were then isolated for GCS applications involving $\mathrm{scCO_2}$ and brine. In GCS, this requires that for an imbibition scenario (trapped $\mathrm{scCO_2}$, injected brine) only wetting angles that are non-wetting $\theta > 90^\circ$ must be considered, owing to the general hydrophilicity of natural shales and sandstones. Similarly, in drainage (trapped brine,

injected $\mathrm{scCO_2}$), only wetting angles $\theta < 90^\circ$ must be considered. For these cases, it was shown that for imbibition, the enhancement or diminishment of permeability depends on the hydrophilicity of the reservoir rock, where, for example, the presence of muscovite ($\theta = 60^\circ$) could enhance permeability and the presence of quartz ($\theta = 20^\circ$) could diminish the permeability, affecting the mobility of $\mathrm{scCO_2}$ ganglia upstream of the pore throat. In mixed-wet systems, this can introduce some complications in the calculation of permeability. In drainage, the presence of quartz and muscovite would permit permeability enhancement. The extreme sensitivity of permeability enhancement or diminishment to the degree of roughness requires that for any affect of interfacial slip to be observed, the roughness ratio must be quite large $\beta > 0.1$. It can be concluded that, in most reservoirs where the estimated surface roughness features are small [*Schlueter et al.*, 1997; *Vallejo et al.*, 2001], the permeability will not be altered in any significant way by the interfacial slip of the trapped residual phases. If however there is a local heterogeneity within the pore that increases the surface roughness feature (e.g. clay deposits), permeability may be enhanced or diminished and, for example, could potentially affect the mobility of $\mathrm{scCO_2}$ ganglia. Although this work was motivated by geologic carbon storage, the results were generalized for arbitrary fluid pairs and wettability and are thus applicable to other subsurface operations involving two-phase flows (e.g., oil recovery, groundwater, geothermal energy, environmental remediation, etc.) as well as to the general field of microfluidics, where sufficiently rough geometries described in this paper could be manufactured.

5 Acknowledgements

This material is based upon work supported as part of the Center for Frontiers of Subsurface Energy Security, an Energy Frontier Research Center funded by the U.S. Department of Energy, Office of Science, Office of Basic Energy Sciences under award DE-SC0001114. Sandia National Laboratories is a multi-mission laboratory managed and operated by National Technology and Engineering Solutions of Sandia, LLC., a wholly owned subsidiary of Honeywell International, Inc., for the U.S. Department of Energy's National Nuclear Security Administration under contract DE-NA-0003525. Readers may access the data presented in this paper by contacting the corresponding author.

References

Al-Menhali, A. S., and S. Krevor (2016), Capillary Trapping of $\mathrm{CO_2}$ in Oil Reservoirs: Observations in a Mixed-Wet Carbonate Rock, *Environmental Science & Technology*, *50*(5), 2727–2734.

Bennion, D. B., and S. Bachu (2006), Supercritical $\mathrm{CO_2}$ and $\mathrm{H_2S}$-Brine Drainage and Imbibition Relative Permeability Relationships for Intercrystalline Sandstone and Carbonate Formations, in *SPE Europec/EAGE Annual Conference and Exhibition*, Society of Petroleum Engineers.

Bobko, C., and F.-J. Ulm (2008), The nano-mechanical morphology of shale, *Mechanics of Materials*, *40*(4), 318–337.

Brady, P. V., N. R. Morrow, A. Fogden, V. Deniz, and N. Loahardjo (2015), Electrostatics and the Low Salinity Effect in Sandstone Reservoirs, *Energy & Fuels*, *29*(2), 666–677.

Broseta, D., N. Tonnet, and V. Shah (2012), Are rocks still water-wet in the presence of dense $\mathrm{CO_2}$ or $\mathrm{H_2S}$?, *Geofluids*, *12*(4), 280–294.

Brown, S. R., and C. H. Scholz (1985), Broad Bandwidth Study of the Topography of Natural Rock Surfaces, *Journal of Geophysical Research*, *90*(B14), 12,575–12,582.

Cairncross, R. A., P. R. Schunk, T. A. Baer, R. R. Rao, and P. A. Sackinger (2000), A finite element method for free surface flows of incompressible fluids in three dimensions. Part I. Boundary fitted mesh motion, *International Journal for Numerical Methods in Fluids*, *33*(3), 375–403.

Cassie, A., and S. Baxter (1944), Wettability of Porous Surfaces, *Transactions of the Faraday Society*, *40*, 546–551.

Chalbaud, C., M. Robin, J. Lombard, F. Martin, P. Egermann, and H. Bertin (2009), Interfacial tension measurements and wettability evaluation for geological CO_2 storage, *Advances in Water Resources*, *32*(1), 98–109.

Chaudhary, K., M. Bayani Cardenas, W. W. Wolfe, J. A. Maisano, R. A. Ketcham, and P. C. Bennett (2013), Pore-scale trapping of supercritical CO_2 and the role of grain wettability and shape, *Geophysical Research Letters*, *40*(15), 3878–3882.

Chaudhary, K., E. J. Guiltinan, M. B. Cardenas, J. A. Maisano, R. A. Ketcham, and P. C. Bennett (2015), Wettability measurement under high P-T conditions using X-ray imaging with application to the brine-supercritical CO_2 system, *Geochemistry, Geophysics, Geosystems*, *16*(9), 2858–2864.

Chiquet, P., D. Broseta, and S. Thibeau (2007), Wettability alteration of caprock minerals by carbon dioxide, *Geofluids*, *7*(2), 112–122.

Davis, A. M., and E. Lauga (2009), Geometric transition in friction for flow over a bubble mattress, *Physics of Fluids (1994-present)*, *21*(1), 011,701.

de Gennes, P., F. Brochard-Wyart, and D. Quere (2004), *Capillarity and Wetting Phenomena: Drops, Bubbles, Pearls, Waves*, Springer.

Derjaguin, B. (1955), Definition of the Concept of and Magnitude of the Disjoining Pressure and Its Role in the Statics and Kinetics of Thin Layers of Liquid, *Colloid J. USSR*, *17*, 191–197.

Dimri, V. P. (2005), *Fractals in Geophysics and Seismology: An Introduction*, Springer.

Duan, Z., and R. Sun (2003), An improved model calculating CO_2 solubility in pure water and aqueous NaCl solutions from 257 to 533 K and from 0 to 2000 bar, *Chemical Geology*, *193*, 257–271.

Elgmati, M. M., H. Zhang, B. Bai, R. E. Flori, Q. Qu, et al. (2011), Submicron-Pore Characterization of Shale Gas Plays, in *North American Unconventional Gas Conference and Exhibition*, Society of Petroleum Engineers.

Espinoza, D. N., and J. C. Santamarina (2010), Water-CO_2-mineral systems: Interfacial tension, contact angle, and diffusion–Implications to CO_2 geological storage, *Water Resources Research*, *46*(7).

Goren, S. L. (1962), The instability of an annular thread of fluid, *Journal of Fluid Mechanics*, *12*(02), 309–319.

Hammond, P. (1983), Nonlinear adjustment of a thin annular film of viscous fluid surrounding a thread of another within a circular cylindrical pipe, *Journal of Fluid Mechanics*, *137*, 363–384.

Herminghaus, S. (2000), Roughness-induced non-wetting, *Europhysics Letters*, *52*(2), 165–170.

Heroux, M., R. Bartlett, R. Howle, J. Hoekstra, J. Hu, R. Kolda, K. Lehoucq, R. Long, E. Pawlowski, A. Phipps, H. Salinger, H. Thornquist, R. Tuminaro, J. Willenbring, and A. Williams (2003), An Overview of Trilinos SAND2003-2927, *Tech. Rep. SAND2003-2927*, Sandia National Laboratories, Albuquerque, NM.

Hysing, S. (2006), A new implicit surface tension implementation for interfacial flows, *International Journal for Numerical Methods in Fluids*, *51*(6), 659–672.

Hyväluoma, J., and J. Harting (2008), Slip Flow Over Structured Surfaces with Entrapped Microbubbles, *Physical Review Letters*, *100*(24), 246,001.

Iglauer, S., A. Paluszny, C. H. Pentland, and M. J. Blunt (2011), Residual CO_2 imaged with X-ray micro-tomography, *Geophysical Research Letters*, *38*(21).

Iglauer, S., A. Salamah, M. Sarmadivaleh, K. Liu, and C. Phan (2014), Contamination of silica surfaces: impact on water–CO_2–quartz and glass contact angle measurements, *International Journal of Greenhouse Gas Control*, *22*, 325–328.

Iglauer, S., C. Pentland, and A. Busch (2015), CO_2 wettability of seal and reservoir rocks and the implications for carbon geo-sequestration, *Water Resources Research*, *51*(1), 729–774.

Iglauer, S., T. Rahman, M. Sarmadivaleh, A. Al-Hinai, M. A. Fernø, M. Lebedev, et al. (2016), Influence of Wettability on Residual Gas Trapping and Enhanced Oil Recovery in Three-Phase Flow: A Pore-Scale Analysis by Use of Microcomputed Tomography, *SPE Journal*.

Jung, J.-W., and J. Wan (2012), Supercritical CO_2 and Ionic Strength Effects on Wettability of Silica Surfaces: Equilibrium Contact Angle Measurements, *Energy & Fuels*, *26*(9), 6053–6059.

Kim, J., and P. Moin (1985), Application of a Fractional-Step Method to Incompressible Navier-Stokes Equations, *Journal of Computational Physics*, *59*(2), 308–323.

Kim, K.-Y., W. S. Han, J. Oh, T. Kim, and J.-C. Kim (2012a), Characteristics of Salt-Precipitation and the Associated Pressure Build-Up During CO_2 Storage in Saline Aquifers, *Transport in Porous Media*, *92*(2), 397–418.

Kim, Y., J. Wan, T. J. Kneafsey, and T. K. Tokunaga (2012b), Dewetting of Silica Surfaces Upon Reactions with Supercritical CO_2 and Brine: Pore-Scale Studies in Micromodels, *Environmental Science & Technology*, *46*(7), 4228–4235.

Korvin, G. (1992), *Fractal Models in the Earth Sciences*, Elsevier Science Ltd.

Krevor, S., R. Pini, L. Zuo, and S. M. Benson (2012), Relative permeability and trapping of CO_2 and water in sandstone rocks at reservoir conditions, *Water Resources Research*, *48*(2).

Krohn, C. E. (1988), Fractal measurements of sandstones, shales, and carbonates, *Journal of Geophysical Research: Solid Earth*, *93*(B4), 3297–3305.

Lake, L. (1989), *Enhanced Oil Recovery*, Englewood Cliffs, New Jersey, USA: Prentice Hall.

Lieu, K. P. (2014), Sediment Diagenesis and Characteristics of Grains and Pore Geometry in Sandstone Reservoir Rocks From a Well of the North German Basin, Ph.D. thesis, Ludwig-Maximilians-Universität.

MacInnis, I. N., and S. L. Brantley (1993), Development of etch pit size distributions on dissolving minerals, *Chemical Geology*, *105*(1), 31–49.

Mandelbrot, B. B. (1983), The Fractal Geometry of Nature.

Marini, L. (2006), *Geological Sequestration of Carbon Dioxide: Thermodynamics, Kinetics, and Reaction Path Modeling*, vol. 11, Elsevier.

Martinez, M. J., and M. A. Hesse (2016), Two-phase convective CO_2 dissolution in saline aquifers, *Water Resources Research*, *52*(1), 585–599.

Meckel, T., S. Bryant, and P. Ganesh (2015), Characterization and prediction of CO_2 saturation resulting from modeling buoyant fluid migration in 2D heterogeneous geologic fabrics, *International Journal of Greenhouse Gas Control*, *34*, 85–96.

Nelson, P. H. (2009), Pore-throat sizes in sandstones, tight sandstones, and shales, *AAPG Bulletin*, *93*(3), 329–340.

Notz, P., S. R. Subia, M. M. Hopkins, H. K. Moffat, and D. R. Noble (2007), Aria 1.5: User Manual SAND2007-2734, *Tech. Rep. SAND2007-2734*, Sandia National Laboratories, Albuquerque, NM.

Pruess, K., and N. Müller (2009), Formation dry-out from CO_2 injection into saline aquifers: 1. Effects of solids precipitation and their mitigation, *Water Resources Research*, *45*(3).

Radke, C., A. Kovscek, H. Wong, et al. (1992), A Pore-Level Scenario for the Development of Mixed Wettability in Oil Reservoirs, in *SPE Annual Technical Conference and Exhibition*, Society of Petroleum Engineers.

Rahman, T., M. Lebedev, A. Barifcani, and S. Iglauer (2016), Residual trapping of supercritical CO_2 in oil-wet sandstone, *Journal of Colloid and Interface Science*, *469*, 63–68.

Reddy, S., P. R. Schunk, and R. T. Bonnecaze (2005), Dynamics of low capillary number interfaces moving through sharp features, *Physics of Fluids*, *17*(12), 122,104.

Rothstein, J. P. (2010), Slip on Superhydrophobic Surfaces, *Annual Review of Fluid Mechanics*, *42*, 89–109.

Rys, F. S., and A. Waldvogel (1986), Fractal shape of hail clouds, *Physical Review Letters*, *56*(7), 784.

Schlueter, E., R. Zimmerman, P. Witherspoon, and N. Cook (1997), The fractal dimension of pores in sedimentary rocks and its influence on permeability, *Engineering Geology*, *48*(3-4), 199–215.

Schmatz, J., J. L. Urai, S. Berg, and H. Ott (2015), Nanoscale imaging of pore-scale fluid-fluid-solid contacts in sandstone, *Geophysical Research Letters*, *42*(7), 2189–2195.

Song, J., and O. J. Rojas (2013), Approaching super-hydrophobicity from cellulosic materials: A Review, *Nordic Pulp & Paper Research*, *28*(2), 216–238.

Spycher, N., K. Pruess, and J. Ennis-King (2003), CO_2-H_2O mixtures in the geological sequestration of CO_2. I. Assessment and calculation of mutual solubilities from 12 to 100 C and up to 600 bar, *Geochimica et Cosmochimica Acta*, *67*(16), 3015–3031.

Steinberger, A., C. Cottin-Bizonne, P. Kleimann, and E. Charlaix (2007), High friction on a bubble mattress, *Nature Materials*, *6*(9), 665–668.

Thomson, W. (1872), 4. On the Equilibrium of Vapour at a Curved Surface of Liquid, *Proceedings of the Royal Society of Edinburgh*, *7*, 63–68.

Treiber, L., W. Owens, et al. (1972), A Laboratory Evaluation of the Wettability of Fifty Oil-Producing Reservoirs, *Society of Petroleum Engineers Journal*, *12*(06), 531–540.

Tuller, M., D. Or, and L. M. Dudley (1999), Adsorption and capillary condensation in porous media: Liquid retention and interfacial configurations in angular pores, *Water Resources Research*, *35*(7), 1949–1964.

Vallejo, L. E., A. Stewart-Murphy, et al. (2001), Influence of pore wall roughness on the slaking of shales, in *DC Rocks 2001, The 38th US Symposium on Rock Mechanics (USRMS)*, American Rock Mechanics Association.

Wang, Y. (2014), Nanogeochemistry: Nanostructures, emergent properties and their control on geochemical reactions and mass transfers, *Chemical Geology*, *378*, 1–23.

Wang, Y., C. Bryan, T. Dewers, J. E. Heath, and C. Jove-Colon (2012), Ganglion Dynamics and Its Implications to Geologic Carbon Dioxide Storage, *Environmental Science & Technology*, *47*(1), 219–226.

Wenzel, R. N. (1936), Resistance of solid surfaces to wetting by water, *Industrial & Engineering Chemistry*, *28*(8), 988–994.

Wong, P.-z., J. Howard, and J.-S. Lin (1986), Surface Roughening and the Fractal Nature of Rocks, *Physical Review Letters*, *57*(5), 637.